**Prediction of Compressive Toughness for Fibre Composites**

M. P. F. Sutcliffe; N. A. Fleck; X. J. Xin

*Proceedings: Mathematical, Physical and Engineering Sciences*, Vol. 452, No. 1954 (Nov. 8, 1996), 2443-2465.

Stable URL:
http://links.jstor.org/sici?sici=1364-5021%2819961108%29452%3A1954%3C2443%3APOCTFF%3E2.0.CO%3B2-V

*Proceedings: Mathematical, Physical and Engineering Sciences* is currently published by The Royal Society.

# Prediction of compressive toughness for fibre composites

By M. P. F. Sutcliffe, N. A. Fleck and X. J. Xin

*Department of Engineering, University of Cambridge, Trumpington St., Cambridge CB2 1PZ, UK*

The development of microbuckling from a sharp notch under remote compressive loading is analysed for a long fibre composite. The composite is modelled as alternating layers of elastic fibres and a nonlinear matrix. A finite element analysis is used to predict microbuckle initiation. The relationship between the compressive mode-I stress intensity factor $K$ and the microbuckle length $\ell$ (that is, the compressive $R$-curve) is calculated. The effect of matrix yield strain on the $R$-curve is significant, while the influence of the matrix strain-hardening rate and initial fibre waviness is slight. $R$-curves predicted by the finite element method agree qualitatively with those predicted using a cohesive zone model, although there are quantitative differences. Prediction of the initiation of microbuckling is found to be in good agreement with experimental data for a carbon fibre epoxy composite.

## 1. Introduction

Long fibre-polymer matrix composites, such as carbon fibres in an epoxy matrix, possess excellent tensile properties resulting from the high tensile strength of the fibres. However, they fail in compression by plastic microbuckling at stresses of only about 60% of their tensile strength (Awerbuch & Madhukar 1985; Soutis *et al.* 1993). Structural components made from long fibre composites typically contain fastener holes and cut-outs; they may also suffer service damage, for example in the form of holes, fibre fractures and delaminations. These imperfections reduce the compressive strength by inducing stress concentrations and by promoting the initiation and propagation of microbuckles. Compressive failure from a hole in a composite laminate has been modelled with varying degrees of sophistication, including the maximum local stress criterion (Peterson 1974), the net section stress criterion, the average stress failure criterion (Nuismer & Labor 1979), the point stress failure criterion (Rhodes *et al.* 1984), the Whitney & Nuismer (1974) model, and more recently the Soutis, Fleck & Smith (Soutis *et al.* 1991) model.

The Soutis, Fleck & Smith (Soutis *et al.* 1991) model is based on the notion of a cohesive zone in which damage around an open hole is represented by a line-crack loaded with a normal compressive traction. The magnitude of the traction is taken to decrease linearly with increasing overlap of the crack faces. Experimental work carried out to study the compressive failure of notched composites (Soutis *et al.* 1991; Soutis *et al.* 1993) has confirmed that compressive failure is governed by plastic microbuckling of the 0° plies and that the Soutis, Fleck & Smith model adequately predicts the effects of hole size and lay-up upon notched compressive strength. This

*Proc. R. Soc. Lond.* A (1996) **452**, 2443–2465
*Printed in Great Britain*

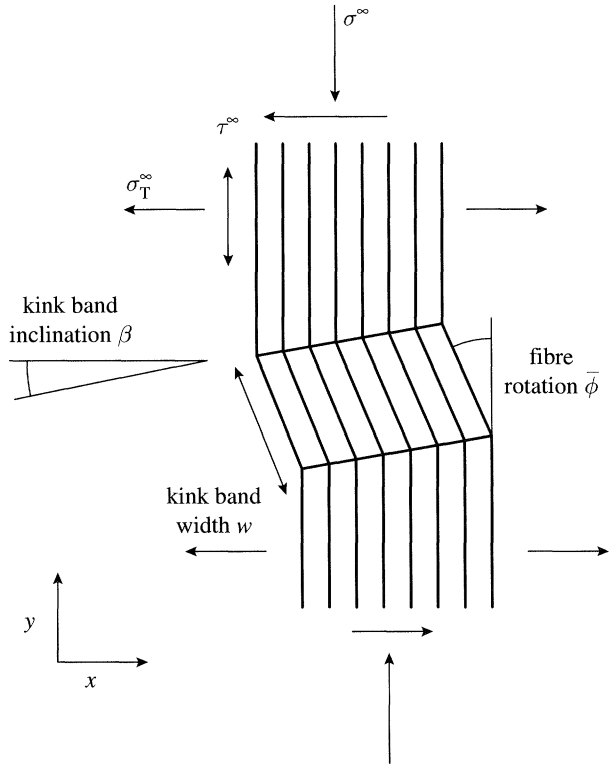


Figure 1. An infinite kink band in a unidirectional composite. Fibres within the band have an initial misalignment angle $\bar{\phi}$.

engineering model takes as its input the compressive fracture toughness and the unnotched strength of the laminate. From the design and manufacturing points of view, it is desirable to predict the unnotched strength and the fracture toughness from the mechanical properties of the basic material constituents: the fibres, matrix and the lay-up geometry.

It is now well-established that the unnotched compressive strength $\sigma_c$ is governed by imperfection-sensitive plastic microbuckling and that the imperfection exists in the form of fibre misalignment (Argon 1972; Budiansky 1983; Budiansky & Fleck 1993; Fleck *et al.* 1993). Slaughter *et al.* (1993) considered microbuckling from an infinite band of uniform fibre misalignment $\bar{\phi}$, as shown in figure 1; the unidirectional composite is subjected to a remote axial stress $\sigma^\infty$ parallel to the fibre direction, an in-plane transverse stress $\sigma_T^\infty$ and an in-plane longitudinal shear stress $\tau^\infty$. The infinite band is inclined with respect to the fibre axes such that the normal to the band is at an angle $\beta$ to the nominal fibre direction, as shown in figure 1. For the case where the composite displays a rigid-perfectly plastic in-plane response the compressive strength is given by

$$\sigma_c \approx \frac{\tau_y - \tau^\infty - \sigma_T^\infty \tan\beta}{\bar{\phi}}, \tag{1.1}$$

where $\tau_y$ is the shear yield strength of the composite (Slaughter *et al.* 1993).

By using the above kinking theory, the unnotched strength of a unidirectional lay-up may be predicted in terms of the shear properties of the composite, the fibre

misalignment angle and the remote multiaxial stress state. On the other hand, a theoretical study of the prediction of compressive fracture toughness has been lacking. The compressive fracture toughness $K_c$ has been measured for a wide range of lay-ups of T800/924C carbon-epoxy material with centre-cracked specimens (Soutis *et al.* 1993). The measured value of $K_c$ is found to be independent of initial notch length, in support of the concept of a compressive fracture toughness. Sutcliffe & Fleck (1993) investigated the effect of the specimen size relative to the bridging length scale $r_p = K_c^2/\sigma_c^2$ on the transition between small-scale and large-scale bridging of notched specimens. They concluded that, if the bridging length scale $r_p$ is small compared with the specimen dimensions, the specimen fails when the stress intensity at the tip of a sharp notch equals a critical compressive stress intensity factor $K_c$. When $r_p$ is not small compared with either the initial notch length or the unnotched ligament then it is necessary to include the details of the crack bridging law in a cohesive zone calculation to predict the failure load accurately.

In the current study, a finite element analysis is used to investigate the initiation and propagation of a microbuckle from the tip of a traction-free crack under remote compressive loading. The analysis is relevant to compressive failure from a sharp notch, where the width of the notch is sufficiently large to ensure that the notch faces do not touch under the compressive loading. An $R$-curve behaviour is predicted whereby the microbuckle length $\ell$ increases with increasing compressive mode-I stress intensity $K_I$. The sensitivity of the $R$-curve to the matrix shear strength, fibre bending stiffness and to the initial fibre waviness is determined. An exploratory study is also conducted into the effect of a superimposed mode-II component on microbuckling. Section 4 describes a large-scale bridging model of microbuckle initiation which uses a crack-bridging law derived from infinite band calculations of microbuckling. $R$-curves calculated using this bridging analysis are compared with $R$-curves predicted by the finite element model.

## 2. Finite element formulation

Consider a composite panel containing a sharp notch under remote compressive loading. If the notch is sufficiently sharp it behaves as an open crack. When the region of nonlinearity at the tip of the crack is small compared to the crack length, the nonlinear region is embedded within the crack tip elastic $K$-field and the condition of 'small scale yielding' is met. Then, the stress field in the vicinity of the crack tip can be determined using a boundary layer formulation: a domain containing a crack is loaded on its outer boundary by a compressive $K$-field of mode-I type. In the present study we make use of the commercial finite element code ABAQUS (1994) to examine the development of microbuckling from the tip of the traction-free crack in a unidirectional composite under a compressive mode-I $K$-field.

### (*a*) *Finite element mesh*

A sketch of the small-scale yielding problem is shown in figure 2*a*. The initial notch is aligned with the $x$-direction and the fibres are parallel to the $y$-direction. A full mesh is employed in order to allow for the existence of non-symmetric crack tip buckling modes. The outer boundary of the mesh is subjected to the displacement field associated with a compressive mode-I stress intensity factor in an orthotropic elastic solid, as given by Paris & Sih (1969). Two distinct regions of mesh are distinguished in figure 2*a*: an outer mesh and an inner mesh (detailed in figure 2*b*). The

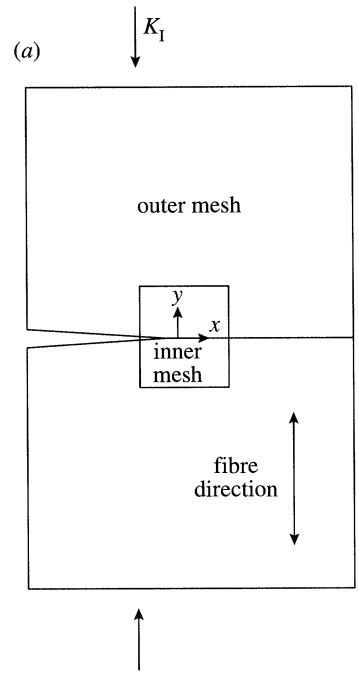


Figure 2. (*a*) Sketch of a unidirectional composite with a semi-infinite crack under a remote mode-I stress intensity factor $K_I$.

inner mesh consists of alternating layers of fibres of thickness $d$, and of matrix of thickness $t$. The relative magnitudes of $d$ and $t$ are chosen to achieve a fibre volume fraction $c = d/(d+t) = \frac{2}{3}$. Since the fibres carry significant bending stresses during microbuckling they are represented by eight-noded quadratic-interpolation elements; the matrix undergoes predominantly plastic shear deformation and is represented by four-noded linear-interpolation elements. For the inner mesh shown schematically in figure 2*b* there are 25 fibres ahead of the crack tip, and six fibres behind the crack tip; the inner zone of the mesh is of height $36d$. The tip of the crack is located at the boundary between a matrix layer and a fibre layer, with a fibre immediately ahead of the crack tip and the adjacent matrix layer immediately behind the crack tip. Unless otherwise stated, all fibres are straight in the undeformed configuration. The outer mesh consists of four-noded linear-interpolation elements with elastic–plastic properties representative of the composite; beam elements are embedded in the outer mesh in order to model the fibre bending resistance and to provide the main contribution to the longitudinal stiffness $E_{yy}$ of the composite.

The full mesh has 6676 elements and the ratio of the inner mesh area to the total mesh area is $3.6 \times 10^{-4}$. Material properties for the inner and outer meshes are given below. Small-scale yielding conditions are maintained by ensuring that the plastic zone size is much less than the overall mesh size.

### (*b*) *Shear properties of the composite*

When the composite is loaded by an in-plane shear stress $\tau$ parallel to the fibre direction, the measured shear strain is well fitted by the Ramberg–Osgood relation

$$\frac{\gamma}{\gamma_y} = \frac{\tau}{\tau_y} + \alpha_c \left(\frac{\tau}{\tau_y}\right)^n, \tag{2.1}$$

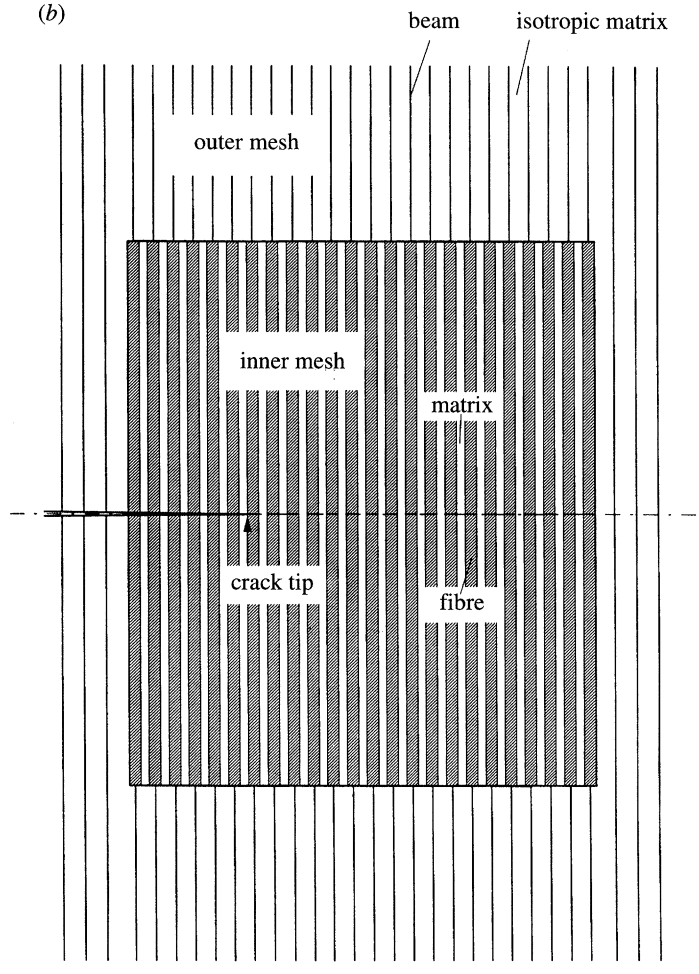


Figure 2. (*b*) Details of the mesh near the crack tip. The inner mesh consists of alternating fibre and matrix elements, while the outer mesh consists of matrix and beam elements.

where $\tau_y$ is the measured composite shear yield strength, $\gamma_y$ is the shear yield strain and $n$ is the strain hardening exponent. The shear modulus $G$ is defined by the initial slope of the measured $\tau$–$\gamma$ curve and equals $\tau_y/\gamma_y$; the Ramberg–Osgood parameter $\alpha_c$ is taken as $\frac{3}{7}$. The material parameters used in our calculations are summarized in table 1. For the majority of the calculations we select the material properties to represent those of unidirectional Toray T800 carbon fibres in a Ciba–Geigy 924C epoxy matrix. This material has been intensively examined within the authors' laboratory (Soutis & Fleck 1990) and its Ramberg–Osgood parameters have been measured by Jelf & Fleck (1994). In the following two sections we develop constitutive relations for the finite elements of the inner and outer mesh, based on the composite shear response (2.1).

### (*c*) *Material properties of the inner mesh*

The fibres are taken to be isotropic and linear elastic, with a Young's modulus of $E_f = 240\ GPa$ and a Poisson's ratio of $\nu_f = 0.32$. These values are typical of Toray T800 carbon fibres, which have a fibre diameter $d = 5\ \mu m$. The properties of the

Table 1. *Materials constants used in the calculations*

(Unless otherwise stated, $n = 3.5$ and $\sigma_y = 108$ MPa ($\gamma_y = 9.2 \times 10^{-3}$), when material properties are typical of unidirectional T800/924C carbon fibre-epoxy material. The properties of the outer mesh beam elements are detailed in § 2.)

| | composite | inner mesh: fibres | inner mesh: matrix | outer mesh: four-noded elements |
|---|---|---|---|---|
| $E_{xx}$ (GPa) | 9.25 | 240 | 6.4 | 18 |
| $E_{yy}$ (GPa) | 162 | isotropic | isotropic | isotropic |
| $G$ (GPa) | 6.8 | 91 | 2.3 | 6.7 |
| $\nu_{xy}$ | 0.0195 | 0.32 | 0.40 | 0.34 |
| $\sigma_y$ ($= \sqrt{3}\tau_y$) (MPa) | 10.8–1080 | — | 10.8–1080 | 10.8–1080 |
| $\alpha$ | $\frac{3}{7}$ | — | $\frac{3}{7}$ | $\frac{3}{7}$ |
| $n$ | 3.5–100 | — | 3.5–100 | 3.5–100 |

matrix in the inner region are chosen so that the overall shear response within the inner region matches the measured response of the composite in shear. The in-plane response of the matrix is modelled by a Ramberg–Osgood nonlinear deformation theory solid. In uniaxial tension the strain $\varepsilon$ in the matrix is related to the tensile stress $\sigma$ by

$$\frac{\varepsilon}{\varepsilon_{Ym}} = \frac{\sigma}{\sigma_{Ym}} + \alpha_m \left(\frac{\sigma}{\sigma_{Ym}}\right)^n, \tag{2.2}$$

where $n$ is the strain hardening exponent, $\sigma_{\mathrm{Ym}}$ is the uniaxial yield strength and $\varepsilon_{\mathrm{Ym}}$ is the yield strain of the matrix. Young's modulus for the matrix is given by $E = \sigma_{\mathrm{Ym}}/\varepsilon_{\mathrm{Ym}}$ and the constant $\alpha_{\mathrm{m}}$ is related to $\alpha_{\mathrm{c}}$ by the argument given below. Assumed properties for the fibres and matrix are summarized in table 1.

Budiansky & Fleck (1993) show how the properties of the composite can be related to the Ramberg–Osgood parameters of the matrix. First, they make the assumptions that the fibres are rigid in shear and that the shear strength $\tau_{ym}$ of the matrix equals that of the composite $t_y$. The uniaxial yield strength of the matrix $\sigma_{ym}$ is given by $\sigma_{ym} = \sqrt{3}\tau_{ym}$. The shear modulus of the matrix $G_m$ is derived from the composite modulus $G$ using the rule of mixtures

$$G_m = (1 - c)G. \tag{2.3}$$

Assuming that the matrix behaves as an isotropic elastic–plastic solid, Young's modulus for the matrix $E_m$ is given by $E_m = 2(1 + \nu_m)G_m$; here we shall take Poisson's ratio for the matrix $\nu_m$ equal to 0.40, obtained by independent tests on a Ciba 924C Geigy matrix (Sutcliffe 1995, personal communication). Fleck & Budiansky (1993) show that the strain-hardening parameter $n$ is the same as for the composite, but that $\alpha_m$ in equation (2.2) should be taken as

$$\alpha_m = \tfrac{2}{3}(1 + \nu_m)\alpha_{\mathrm{c}}. \tag{2.4}$$

In practice in our finite element simulations we do not make the small correction (2.4) but take $\alpha_m = \alpha_{\mathrm{c}} = \frac{3}{7}$.

### (*d*) *Material properties of the outer mesh*

Limitations of computer memory and computation time preclude modelling of the outer mesh by alternating layers of fibre and matrix elements. Instead, the outer mesh is modelled by a combination of four-noded elements and line-beam elements. The tangent stiffness matrices of these two elements will then be summed to provide the effective tangent stiffness matrix for the composite in the outer mesh.

The four-noded elements are modelled as an isotropic deformation theory solid that is consistent with the Ramberg–Osgood shear response (2.1) of the composite. Young's modulus $E$ for the four-noded elements is related to $G$ by the isotropic relation $E = 2(1 + \nu)G$. Here, Poisson's ratio is taken to be that of the composite for straining in the axial $y$-direction.

Now consider the beam elements in the outer mesh. The axial stiffness and bending stiffness of the beam elements are deduced as follows. The contribution of the fibres to the axial stiffness of the composite is given by $cE_\mathrm{f}$ where $E_\mathrm{f}$ is the longitudinal modulus of the fibres and $c$ is the fibre volume fraction. The fibres also endow the composite with a bending stiffness. Simple beam theory for rectangular fibres of in-plane width $d$, Young's modulus $E_\mathrm{f}$ and volume fraction $c$ gives the relation between the couple stress per unit area $m$ in the composite and the associated curvature $\mathrm{d}\phi/\mathrm{d}y$ as

$$m = \frac{cE_\mathrm{f}d^2}{12}\frac{\mathrm{d}\phi}{\mathrm{d}y}, \tag{2.5}$$

where $\phi$ is the fibre rotation and the $y$-axis is aligned with the fibre direction. In the related study of Fleck *et al.* (1993), the fibre section is taken to be circular and the factor in (2.5) is 16 rather than 12. In the present study we consider two-dimensional alternating layers of fibres and matrix, and it is consistent to consider the fibres as having a rectangular section.

Consider an array of beam elements of spacing $L$ embedded within the four-noded elements of the outer finite element mesh; the beam elements are aligned with the fibre direction. Suppose that the axial modulus for the material of each beam is $E_\mathrm{b}$, its second moment of area is $I_\mathrm{b}$, and its in-plane width is $d_\mathrm{b}$. Then, in order for the mesh to possess the desired axial stiffness and bending stiffness of the composite, the following relationships are enforced:

$$E_\mathrm{b}d_\mathrm{b} = cLE_\mathrm{f} \tag{2.6}$$

and

$$E_\mathrm{b}I_\mathrm{b} = \tfrac{1}{12}cLE_\mathrm{f}d^2. \tag{2.7}$$

Since one can specify independently all three parameters $E_\mathrm{b}$, $d_\mathrm{b}$ and $I_\mathrm{b}$ for a beam element in the finite element calculation, it is necessary to fix arbitrarily one of these three parameters. A simple approach is to assume that Young's modulus of the beam equals that of the fibre, $E_\mathrm{b} = E_\mathrm{f}$. Then, the beam section area and the second moment of area must satisfy the identities $d_\mathrm{b} = cL$ and $I_\mathrm{b} = \frac{1}{12}cLd^2$ with $c$ equal to the measured value of $\frac{2}{3}$ for T800/924C composite.

In order to embed the beam elements within the four-noded linear elements of the outer mesh, shared nodes are tied. In the region of mesh gradation, the smaller elements are tied to the larger elements using the 'linear tie' option within ABAQUS: the nodes of the smaller elements are constrained to deform according to a linear interpolation scheme between the nodes of the neighbouring larger elements. Attention is also paid to ensure continuity of fibre rotation at the transition between the inner

and outer meshes. This is achieved by placing beam elements along the ends of the eight-noded fibre elements at the boundary of the inner mesh. The additional beam elements are of length equal to the width of the eight-noded fibre elements and are ascribed a high bending stiffness (three orders of magnitude higher than that of the beam elements of the outer mesh). The mid-node of each additional beam element is tied to the end of the beam elements of the outer mesh.

## 3. Finite element predictions of microbuckle initiation

Finite element results are now presented for the initiation of a microbuckle from a sharp notch. First, results are given for the evolution of the stress and deformation fields as a function of remote $K_{\mathrm{I}}$. The sensitivity of the microbuckling response to composite material yield strength, strain hardening exponent and the magnitude of initial fibre misalignment is then examined. The section concludes with an examination of the knock-down in microbuckling response when a small mode-II stress intensity is superposed on the compressive mode-I stress intensity.

### (*a*) *Development of microbuckling from the notch tip*

Details of the microbuckle development are presented in this section, with material properties chosen to represent a unidirectional T800/924C carbon fibre-epoxy composite. The deformed mesh is shown in figure 3 at three levels of applied $K_{\mathrm{I}}$, labelled A, B and C. Under increasing compressive $K_{\mathrm{I}}$, the fibres near the crack tip rotate and the matrix suffers combined shear and transverse straining. At low levels of applied load (such as state A, $K_{\mathrm{I}}/G\sqrt{d} = 1.8$) the deformation state is nearly symmetric about the crack plane. The crack profile is shown by overlapping of traction-free crack flanks behind the tip. At a higher load (state B, $K_I/G\sqrt{d} = 2.6$) a pronounced buckle develops at the crack tip; the buckle is asymmetric with respect to the crack plane. Under a further increase in $K_{\mathrm{I}}$, the buckle spreads in the transverse $x$-direction and can be considered to be composed of two microbuckles inclined at $\pm 20°$ with respect to the transverse $x$-direction, as shown by state C in figure 3. Nucleation of the microbuckle involves large tensile transverse strains in the matrix layer surrounding the crack tip. The current analysis includes neither failure of the matrix nor of the fibres: if transverse failure of the matrix were to be incorporated into the analysis then a split would develop at the crack tip, and blunt the stress concentrating effects of the crack tip. In practical carbon fibre-epoxy laminates, off-axis plies lie adjacent to the 0°-plies and prevent split formation under compressive loading (Soutis *et al.* 1993). Since the purpose of the work is to explore microbuckle development in the 0°-plies and so provide insight into the compressive response of practical multidirectional laminates, split development was not investigated further.

To deduce the relationship between the extent of microbuckling and the level of compressive $K_{\mathrm{I}}$ we need to define the boundary of the microbuckle zone. Microbuckling results in a drop in the load carrying capacity of the fibres. The microbuckle length is determined by comparing the mean axial stress in the composite directly ahead of the crack tip with the axial stress associated with the compressive mode-I elastic $K$ field†. This comparison is illustrated in figure 4. At the lowest load (state

† To facilitate the method, the mean axial stress distribution in the composite was found by multiplying the axial strain in the beam elements and at the centre of fibres directly ahead of the crack by the axial modulus of the composite.

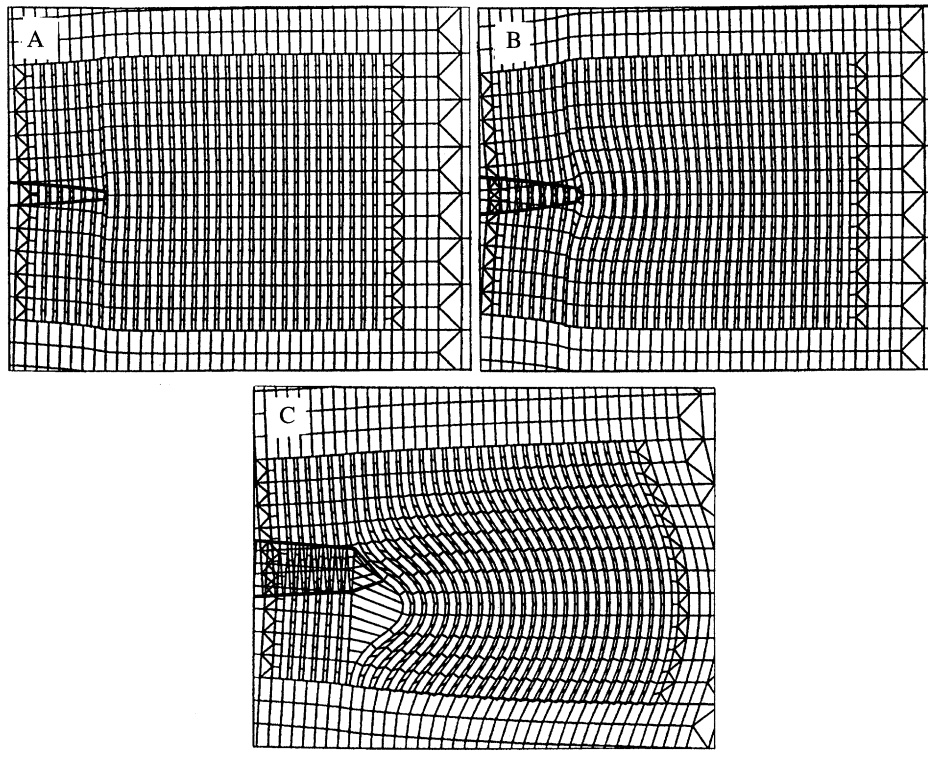


Figure 3. The deformed mesh at three stages of compressive loading. No amplification of deformation is displayed. The states A–C are marked on figure 5*a*.

A) the stress distribution is very nearly that of the elastic solution. At an increased load (state B) the axial stress falls slightly below the elastic value near the crack tip. As the load is increased further (state C) the stresses fall below the elastic solution for a considerable region ahead of the crack tip. We arbitrarily define the extent of the microbuckle as the region where the axial stress lies more than 10% below the elastic stresses. The locations of the microbuckle tip at the various loads are marked by arrows on figure 4. Using this definition of microbuckle length, the finite element calculations show that a finite load is required for microbuckle initiation, just above that of state A. The value of this initial load will depend on the details at the tip; for example, this load will depend on the initial crack tip geometry.

The projected length of the buckle $\ell$ along the transverse $x$-direction is plotted as a function of $K_{\mathrm{I}}$ in figure 5*a*: we refer to this plot as the compressive $R$-curve for the composite. States A to C, illustrated in figure 3, are marked on the corresponding curve in figure 5*a* with $n = 3.5$. A local maximum in the $R$-curve is observed at $K_I/G\sqrt{d} = 2.6$ (corresponding to state B of figure 3*b*). In order to capture this snap-back phenomenon under prescribed $K$-loading, the Riks' algorithm is used within the ABAQUS (1994) program.

(*b*) *Effects of material properties and initial fibre misalignment on the R-curve*

Infinite band calculations on the initiation of microbuckling (Fleck & Budiansky 1991; Budiansky & Fleck 1993) suggest that the unnotched compressive strength increases linearly with the shear strength of the matrix and is inversely proportional

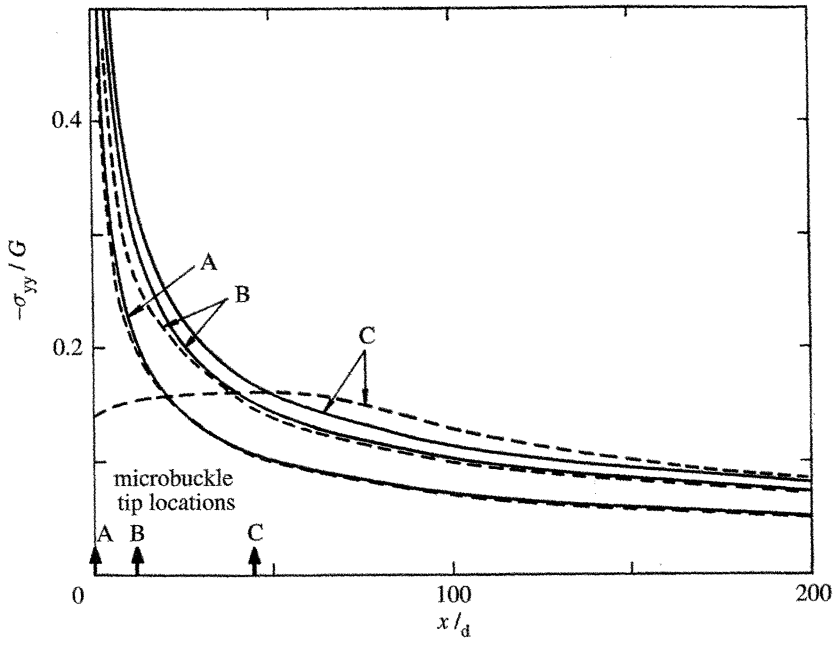


Figure 4. The distribution of mean axial component of stress $\sigma_{yy}$ in the composite immediately ahead of the crack tip, along the line $y = 0$. The stress distribution is given at three stages of loading, corresponding to states A–C of figure 5*a*. —— $K$ field, - - - - finite element results.

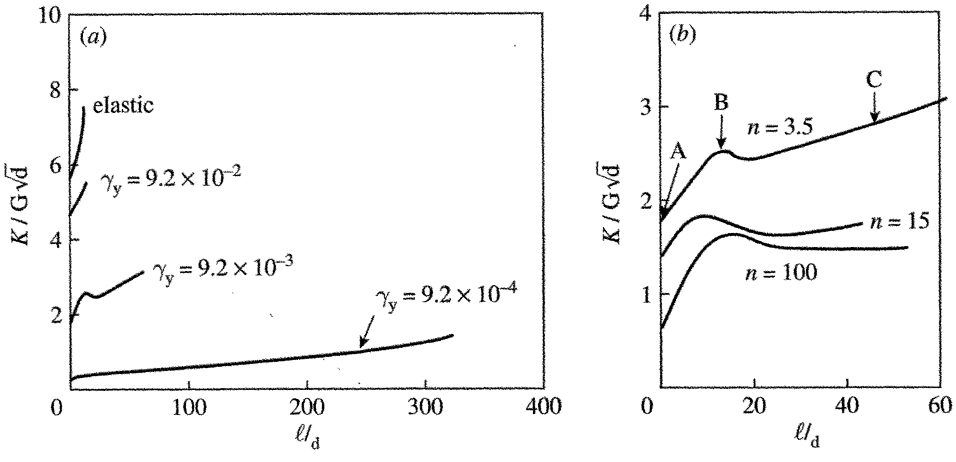


Figure 5. (*a*) $K_I/G\sqrt{d}$ versus projected microbuckle length $\ell$ for a range of values of the Ramberg–Osgood exponent $n$. $\gamma_y = 9.2 \times 10^{-3}$. (*b*) $K_I/G\sqrt{d}$ versus projected microbuckle length $\ell$ for a range of values of shear yield strain $\gamma_y$. $n = 3.5$.

to the degree of fibre misalignment $\bar{\phi}$, as given by relation (1.1). Budiansky & Fleck (1993) demonstrate that the infinite band compressive strength is relatively insensitive to the strain hardening exponent $n$. In this section we explore whether these infinite band findings also hold for microbuckle initiation from a sharp notch.

Figure 5*a* shows that the strain hardening exponent has only a moderate influence on the magnitude of the $R$-curve. With $\gamma_y$ fixed at $9.2 \times 10^{-3}$, the normalized load $K_I/G\sqrt{d}$ required for a given microbuckle length decreases by a factor of about two when $n$ is increased from 3.5 to 100. In figure 5*b*, $R$-curves are given for a range of

values of the shear yield strain $\gamma_y$, with the strain hardening exponent $n$ held fixed at 3.5. Since the shear modulus $G$ is the same for each curve, a change in the value of $\gamma_y \equiv \tau_y/G$ reflects a change in the value of the shear yield strength. Figure 5*b* also includes results for an elastic matrix. We note that the magnitude of $\gamma_y$ has a significant influence on the $R$-curve.

Sutcliffe & Fleck (1994) have measured the $R$-curve associated with in-plane microbuckling of T800/924C unidirectional composite. An initiation compressive fracture toughness of $K_{\mathrm{I}} = 42\,\mathrm{MPa\,m^{1/2}}$ is deduced from their raw data (figure 5 of Sutcliffe & Fleck 1994), corresponding to a value of $K_I/G\sqrt{d} = 2.76$. This is in good agreement with the predicted snap-back value for $K_I/G\sqrt{d}$ of 2.6 found from the finite element calculations, see figure 5*a*.

Next, we examine the effect of fibre misalignment on the compressive $R$-curve. Long fibre composites usually contain fibre misalignment or waviness, typically of the order of 2–3° for polymer matrix systems (Yugartis 1987). The compressive response is examined for two meshes. For both meshes, the fibre misalignment angle $\bar{\phi}$ is ascribed the profile $\bar{\phi} = \phi_0 \sin(\pi y/w_y)$ within a rectangular region surrounding the crack tip, with $w_y = 12d$. The crack tip is placed within this region of local waviness, such that the crack tip butts against a fibre layer and there are two wavy fibres to the left of the crack tip and seven to the right. In mesh I, $\phi_0 = 2.3°$, and in mesh II $\phi_0 = -2.3°$: we describe these as 'forward' and 'backward' waviness respectively. Both meshes are illustrated in figure 6*a*.

Results for meshes I and II are compared with the $R$-curve for the original mesh (containing perfectly aligned fibres) in figure 6*b*. It can be seen that the initial waviness changes only the details in the vicinity of the snap-back buckling load. Mesh II with backward waviness displays the strongest snap-back response at the local maximum in the $K_{\mathrm{I}}$–$\ell$ response and mesh I with forward waviness shows the lowest strength at this point. This is consistent with the observation that the distribution of initial fibre misalignment of mesh I is qualitatively of the same shape as the fibre rotation distribution in state B of figure 3. The initial fibre misalignment of mesh II is of opposite sign to the deformed fibre shape in state B: a snap-through event occurs in order to pop-in the fibre rotation into the shape given in figure 3*b*.

### (*c*) *Estimated K value for fibre failure*

It is found experimentally (Soutis & Fleck 1990) that the width of a microbuckle band is set by fibre fracture in tension due to local fibre bending. It is instructive to post-process the finite element results to determine the maximum tensile strain $\varepsilon_{\max}$ in the fibres ahead of the crack† as a function of the applied $K_{\mathrm{I}}$. The maximum tensile strain is plotted as a function of $K_{\mathrm{I}}$ in figure 7*a* for various values of shear yield strain (with $n = 3.5$), and in figure 7*b* for various values of strain hardening exponent $n$ (with $\gamma_y = 9.2 \times 10^{-3}$). At low levels of applied $K_{\mathrm{I}}$ the strain due to bending in the fibres is less than the mean axial compressive strain in the fibres, hence the maximum fibre strain is negative. At larger values of $K_{\mathrm{I}}$ the maximum fibre strain $\varepsilon_{\max}$ becomes tensile due to increased bending of the fibres‡. We note that large tensile values of maximum axial strain $\varepsilon_{\max}$ develop in the vicinity of the

† The precise location in the fibre layers at which the axial strain component $\varepsilon_{yy}$ is a maximum is dependent upon the magnitude of $K_{\mathrm{I}}$. In general, it occurs in the first fibre placed immediately ahead of the crack tip, although not necessarily straight ahead of the crack.

‡ The loops in the curves for $\gamma_y = 9.2 \times 10^{-3}$ shown in figures 7*a*, *b* are associated with unloading of the first fibre of the crack at the pop-in buckling load.

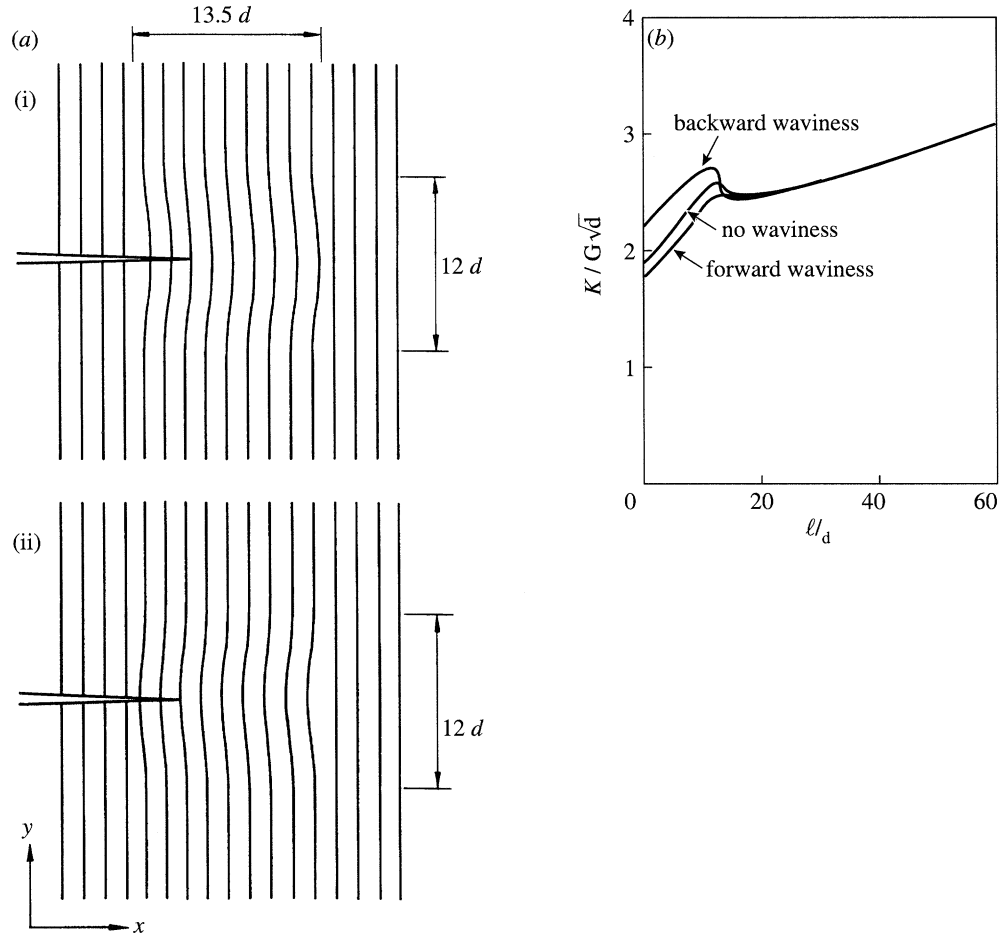


Figure 6. (*a*) Sketches of initial fibre waviness in the crack tip region. The waviness in the $x$-direction is exaggerated by a factor of four: (i) 'forward waviness' and (ii) 'backward waviness'. (*b*) $K_{\mathrm{I}}/G\sqrt{d}$ versus projected microbuckle length $\ell$ for forward and backward waviness.

pop-in buckling load (state B of figure 3). Since the tensile failure strain of carbon fibres is typically 2–3%, fibre fracture is predicted in all cases. Recall from figures 5*a*, *b* that the $K_{\mathrm{I}}$ level to achieve a given length of buckle $\ell$ increases with increasing $\gamma_y$ and decreasing $n$. These features are reflected in the plot of $K_{\mathrm{I}}/G\sqrt{d}$ versus $\varepsilon_{\max}$: for a fixed value of $\varepsilon_{\max}$, $K_{\mathrm{I}}/G\sqrt{d}$ increases with increasing $\gamma_y$ and with decreasing $n$.

### (*d*) *Effect of mode-mix on buckling response*

Since microbuckling is essentially a shear instability it might be expected that in-plane remote shear would seriously degrade the compressive strength. Equation (1.1) for the infinite band unnotched compressive strength predicts that the axial strength $\sigma_{\mathrm{c}}$ decreases to zero as the remote shear stress $\tau^{\infty}$ is increased to the shear yield strength $\tau_y$ of the composite.

$R$-curves for pure mode-I loading and for combined mode-I and II loading are given in figure 8*a*, plotting the mode-I component of load $K_I/G\sqrt{d}$ against the microbuckle length $\ell$. The microbuckle length was again estimated by considering

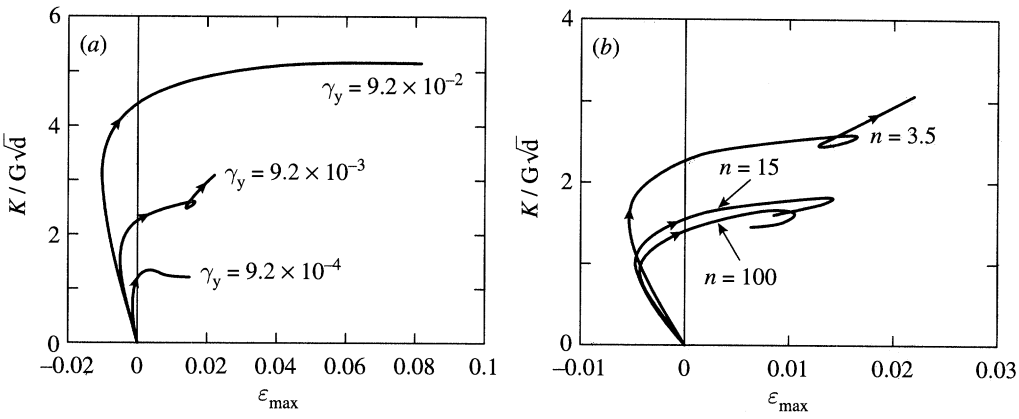


Figure 7. (*a*) Maximum axial strain in the fibres throughout the mesh $\varepsilon_{max}$ as a function of $K_I/G\sqrt{d}$ for a range of values of shear yield strain $\gamma_y$, with $n = 3.5$. Note that $\varepsilon_{max}$ is compressive at low loads, but then becomes tensile with increasing load. (*b*) Maximum fibre strain $\varepsilon_{max}$ as a function of $K_I/G\sqrt{d}$ for a range of values of the Ramberg–Osgood exponent $n$, with $\gamma_y = 9.2 \times 10^{-3}$.

stresses directly ahead of the crack tip. We note that the addition of a 10% mode-II component superimposed on the mode-I component affects the initial part of the *R*-curve but that, once the microbuckle is initiated, the *R*-curve lies close to that without a mode-II component. This behaviour is qualitatively different from the infinite band response (1.1).

The development of microbuckling from the crack tip is shown in figure 8*b* for the case of compressive mode-I loading with a superimposed 10% mode-II component. The deformed mesh is given at the three states of loading A, B and C marked on the *R*-curve of figure 8*a*. It is noted that the presence of the mode-II component deactivates the microbuckle oriented at 20°.

### (*e*) *Discussion*

In our finite element study we have neglected the effect of fibre fracture on the microbuckling collapse. Moran *et al.* (1994) have recently found that fibre fracture does not accompany microbuckle growth in IM8 carbon fibres/PEEK matrix composites. Experimental observations in the authors' laboratory of a number of carbon fibre composites confirm these findings and show that the observed *R*-curve is relatively insensitive to the occurrence of fibre fracture. We surmise that the above finite element calculations of the early stages of microbuckle initiation will remain accurate when the first few fibres near the crack tip do suffer fracture during microbuckling.

It is commonly observed during microbuckling that fibres behind the microbuckle tip rotate by twice the band angle $\beta$ and then 'lock up'. The role of lock-up of the matrix has been ignored in the current analysis and would need to be considered in more detail to be able to calculate the evolution of the microbuckle beyond the initiation phase.

## 4. Large scale bridging model of compressive failure

Crack bridging models have had notable success in the prediction of damage from notches in engineering materials under remote tension. They have also been used to estimate the development of microbuckling from a hole in a composite under compres-

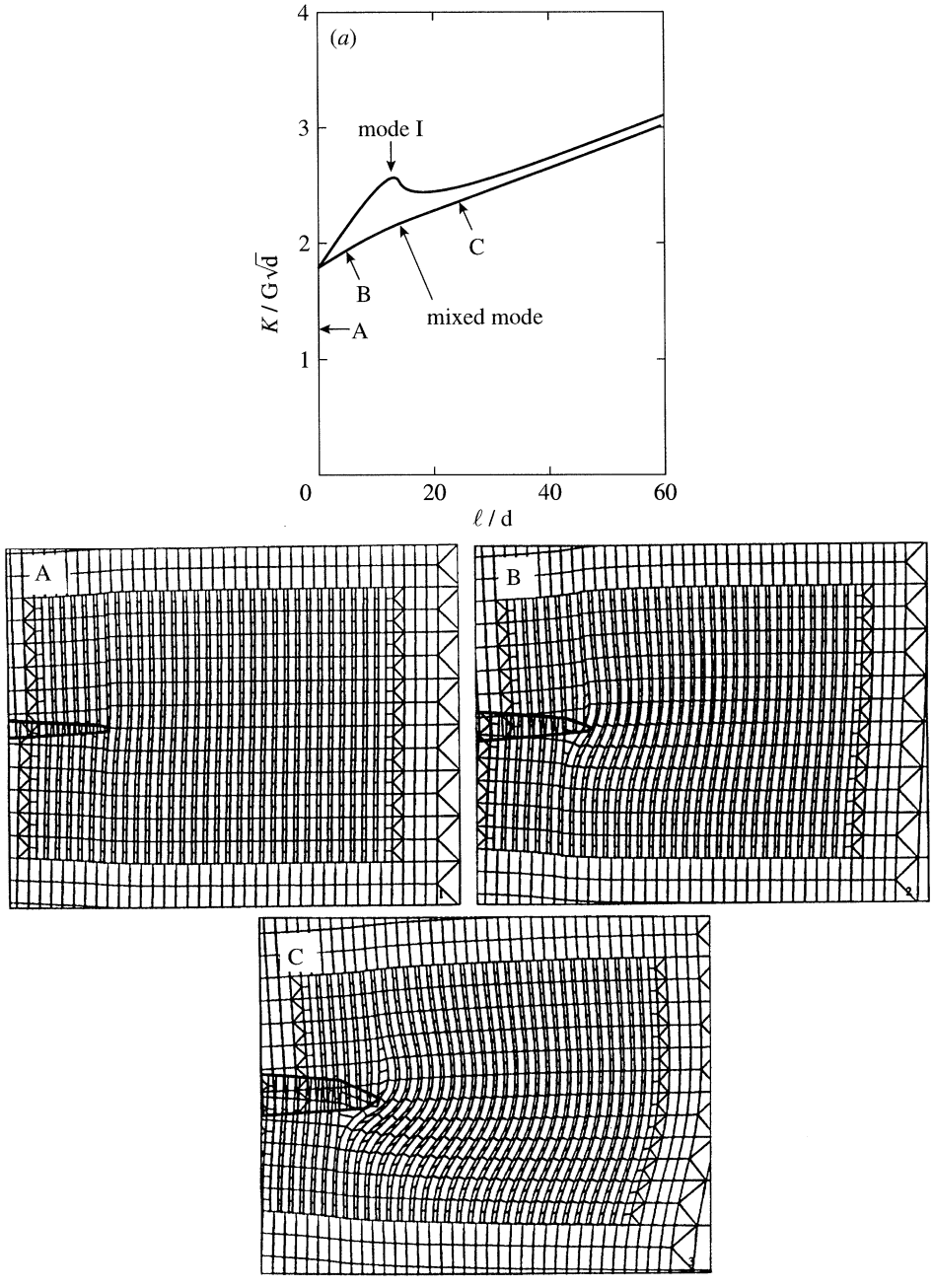


Figure 8. (*a*) Effect of mode mix upon microbuckle growth. The projected microbuckle length is plotted against the applied stress intensity factor $K_{\mathrm{I}}/G\sqrt{d}$ for mode-I loading and for mixed-mode loading with $K_{\mathrm{II}}/K_{\mathrm{I}} = 0.1$. (*b*) The deformed mesh for mixed-mode loading with $K_{\mathrm{II}}/K_{\mathrm{I}} = 0.1$. The mesh is shown at three stages of loading corresponding to states A–C marked in figure 8*a*. No amplification of deformation is displayed.

sion (Soutis *et al.* 1991; Sutcliffe & Fleck 1993). The usual strategy is to concentrate the inelastic deformation associated with plasticity, cracking, microbuckling and so on within a crack and to assume some form of traction-displacement bridging law

across the crack faces. For example, in the Dugdale analysis of plastic yielding in metals from the root of a notch, it is assumed that the bridging normal traction across the crack faces equals the tensile yield strength of the solid. The material response elsewhere in the cracked specimen or structure is assumed to be linear elastic.

Here we shall compare the $R$-curves calculated by the finite element analysis with $R$-curves predicted by crack bridging calculations. The appropriate crack traction-displacement law is derived from the infinite band collapse response of the composite.

### (*a*) *Calculation of crack bridging law*

The crack bridging law is derived from an infinite band calculation of fibre microbuckling as follows. In the infinite band calculation we determine the collapse response of a long panel of composite containing an initial infinite band of fibre waviness. The extra remote displacement $\Delta v$ associated with the microbuckle under a remote stress $\sigma^{\infty}$ is defined by the end shortening of the panel minus the contribution from elastic shortening. Consider the crack bridging law associated with microbuckling from the root of a sharp notch. Since two microbuckles develop at inclinations $\pm\beta$ from the notch root we assume that the crack traction $T$ versus crack overlap $2v$ bridging law equals the remote stress $\sigma^{\infty}$ versus twice the extra remote displacement response $2\Delta v$ of the single infinite band.

Fleck & Shu (1995) have recently developed a finite strain finite element formulation of fibre microbuckling. The in-plane combined shear and transverse response of the composite is taken to be that of a deformation theory elastic–plastic solid with Ramberg–Osgood hardening behaviour described by equation (2.1). The axial response of the composite is taken to be linear elastic and the fibres provide the composite with a finite bending resistance. A couple stress formulation is used to account for the moment-curvature relation (2.5) of the fibres.

The finite element formulation of Fleck and Shu (1995) has been used to calculate the infinite band collapse response for the geometry shown in figure 1. The initial imperfection is taken to consist of an infinite band of misaligned fibres; the normal to the band is inclined at an angle of $\beta = 20°$ with respect to the remote fibre direction. Fibres outside the band are initially straight, and fibres within the band are given an initial misalignment $\phi = \phi_0 \cos \pi y/w$ for $|y| \leqslant \frac{1}{2}w$. The initial width of the band $w$ is taken to be $w = 20d$. This value is representative of observed kink band widths. Although the maximum strength of the infinite band is sensitive to the value assumed for $\phi_0$, the post-critical collapse response is almost insensitive to $\phi_0$. Since we shall use the crack bridging analysis to examine the development of a microbuckle in initially straight fibres we require the infinite band collapse response for initially straight fibres. Upon loading the perfect composite, an elastic bifurcation occurs when $\sigma^{\infty}$ attains the Rosen value of the in-plane shear modulus $G$; thereafter $\sigma^{\infty}$ drops steeply with increasing $\Delta v$. Numerical convergence difficulties were encountered in calculating the initial post-collapse response for the case of perfectly straight fibres; adequate accuracy for the post-collapse response is achieved by assuming a small value for $\phi_0$ of 0.1°. Further details on the calculation procedure for the infinite band are given in Shu & Fleck (1995). The infinite band collapse response can be written in the non-dimensional form

$$\frac{\sigma^{\infty}}{G} = f\left(\frac{\Delta v\sqrt{G}}{d\sqrt{E_{yy}}}, \gamma_y, n, \beta, \frac{E_{xx}}{G}\right), \tag{4.1}$$

where, unless otherwise stated, we take $\gamma_y = 9.2 \times 10^{-3}$, $n = 3.5$ and $E_{xx}/G = 1.36$.

These values have been chosen to give the same constitutive response as that assumed in the finite element calculations of § 3. The collapse response is given in figure 9*a* for a range of strain hardening exponents and in figure 9*b* for a range of shear yield strains. Typically, the collapse response consists of a monotonically decreasing stress $\sigma^{\infty}$ with increasing end shortening $\Delta v$ of the structure. With continued end shortening, a state of steady-state band broadening is achieved, whereby end shortening is associated with broadening of the band of rotated fibres. Within the band the fibre rotation is uniform. Recent experimental observations of this steady-state band broadening phenomenon have been made by Moran *et al.* (1995). The non-dimensional collapse response is sensitive to the value of $\gamma_y$: the post-collapse load increases by a factor of about 20 when $\gamma_y$ is increased from $9.2 \times 10^{-4}$ to $9.2 \times 10^{-2}$, see figure 9*b*. In contrast, the collapse response is relatively insensitive to the value assumed for the strain hardening exponent $n$: as $n$ is increased from 3.5 to 100, the collapse load drops by at most a factor of three, see figure 9*a*.

### (*b*) *Bridging analysis*

The finite element analysis of § 3 was used to estimate the $R$-curve associated with buckling from an initial crack under a remote compressive mode-I stress intensity factor $K_{\mathrm{I}}$. Buckling from the initial crack is by the growth of two microbuckles oriented at $\pm 20^{\circ}$ with respect to the plane of the crack. In the cohesive zone model we replace the pair of microbuckles by a single cohesive zone with appropriate crack bridging law as detailed subsequently.

We use the infinite band response (4.1) as the nonlinear crack bridging law in the cohesive zone calculation: the normal traction $T$ across the crack faces of the cohesive zone is assumed to equal the remote compressive stress $\sigma^{\infty}$ of the infinite band calculation. Since, in the finite element model for compressive fracture, there are two inclined microbuckles emanating from the initial crack, we model the crack face overlap $2v$ of the cohesive zone by twice the remote extra displacement of the infinite band calculation $2\Delta v$. Thus the crack bridging law in the cohesive zone model follows from (4.1) as

$$\frac{\sigma^{\infty}}{G} = f\left(\frac{\Delta v\sqrt{G}}{d\sqrt{E_{yy}}}, \gamma_y, n, \beta, \frac{E_{xx}}{G}\right). \tag{4.2}$$

The general calculation method for the cohesive zone model has been described by Cox & Marshall (1991) and further numerical details are given by Sutcliffe & Fleck (1993). Consider a semi-infinite crack with a cohesive zone existing over a length $\ell$ back from its tip. The normal compressive traction on the crack faces within the cohesive zone is designated $T(x)$, where $x$ is the distance back from the crack tip to the point of interest.

The stress intensity factor $K_{\mathrm{T}}$ due to a distribution of normal traction $T(x)$ over the cohesive zone of length $\ell$ is given by the integral

$$K_{\mathrm{T}} = \int_0^{\ell} T(x)m(x)\,\mathrm{d}x. \tag{4.3}$$

Here, the weight function $m(x)$ is the crack tip stress intensity factor for a pair of unit point loads placed on the crack faces a distance $x$ from the crack tip, and acting normal to the plane of the crack. For a semi-infinite crack in an infinite general anisotropic body, Sih *et al.* (1965) show that this weight function is identical to the

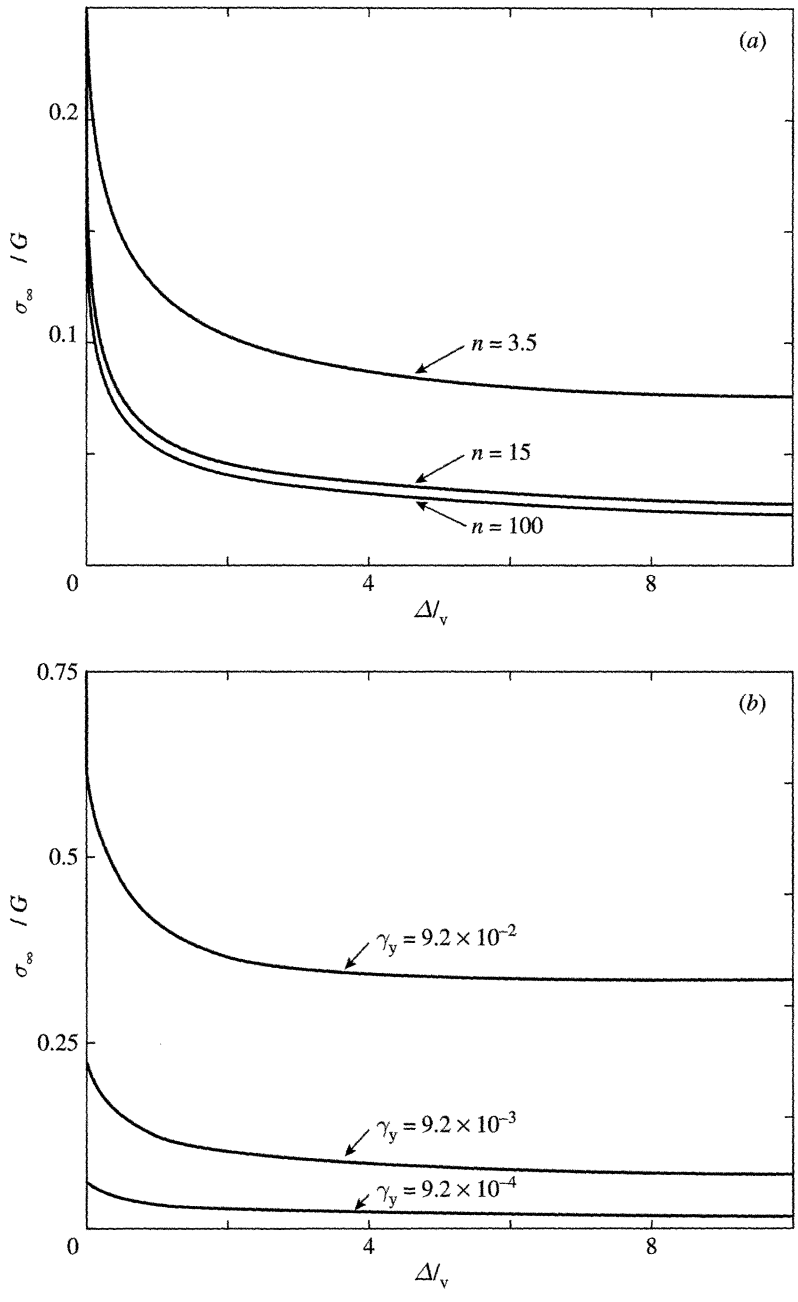


Figure 9. Infinite band collapse response in the form of remote axial stress $\sigma^\infty$ versus extra remote displacement $\Delta v/d$, for a single infinite band inclined at an angle $\beta = 20°$. (*a*) Effect of magnitude of strain hardening exponent $n$ on response, for $\gamma_y = 9.2 \times 10^{-3}$; (*b*) effect of magnitude of yield strain $\gamma_y$ on response, for $n = 3.5$.

isotropic weight function, given by Tada *et al.* (1985) as

$$m(x) = \sqrt{2/\pi x}. \tag{4.4}$$

The crack opening profile $v_T(x)$ of the cohesive zone (i.e. half of the crack opening

displacement), due to a normal compressive traction $T(x)$ on the faces of the crack, is given by

$$v_{\mathrm{T}}(x) = \frac{1}{E'} \int_0^{\ell} T(x')h(x,x')\,\mathrm{d}x', \tag{4.5}$$

where the equivalent elastic modulus $E'$ is defined by

$$\frac{1}{E'} = \left(\frac{1}{2E_{xx}E_{yy}}\right)^{1/2} \left[\left(\frac{E_{yy}}{E_{xx}}\right)^{1/2} - \nu_{yx} + \frac{E_{yy}}{2G}\right]^{1/2}, \tag{4.6}$$

and $h(x,x')$ is the Green's function for the crack face displacement along the crack flanks at a position $x'$ due to a pair of crack wedging forces of unit magnitude at $x$. When the crack lies along a principal material axis of an orthotropic material, the weight function method described by Paris *et al.* (1976) can be used to show that $h$ for the orthotropic material is again identical to the isotropic form

$$h(x,x') = \frac{2}{\pi} \ln \left| \frac{\sqrt{x} + \sqrt{x'}}{\sqrt{x} - \sqrt{x'}} \right|. \tag{4.7}$$

The crack displacement profile $v_K$ due to the remote applied stress intensity factor $K^{\infty}$ is (Tada *et al.* 1985)

$$v_K(x) = \frac{4K^{\infty}\sqrt{x}}{E'\sqrt{2\pi}}. \tag{4.8}$$

We assume that stresses are bounded within the solid so that the total stress intensity factor vanishes at the tip of the cohesive zone, thus

$$K^{\infty} + K_{\mathrm{T}} = 0. \tag{4.9}$$

Relation (4.9) is used below to solve for the length of the cohesive zone length $\ell$ as a function of $K^{\infty}$. In order to solve for the traction distribution within the cohesive zone we set up an integral equation in $T(x)$ as follows. The crack face overlap displacement $2v$ due to the crack tractions $T$ and to the remote load $K^{\infty}$ follows from (4.5) and (4.8) as

$$v(x) = v_K + v_{\mathrm{T}} = \frac{4K^{\infty}\sqrt{x}}{E'\sqrt{2\pi}} + \frac{2}{\pi E'} \int_0^{\ell} T(x) \ln \left| \frac{\sqrt{x'} + \sqrt{x'}}{\sqrt{x'} - \sqrt{x'}} \right| \mathrm{d}x. \tag{4.10}$$

Now, the crack overlap displacement $2v$ is related to the compressive traction $T$ across the cohesive zone by the inverse of relation (4.2), which we rewrite as

$$\frac{v\sqrt{G}}{d\sqrt{E_{yy}}} = f^{-1}\left(\frac{T}{G}\right). \tag{4.11}$$

Relations (4.10) and (4.11) may be combined to give an integral equation in $T$, which in non-dimensional form appears as

$$f^{-1}\left(\frac{T(\xi)}{G}\right) = 4\left(\frac{\ell G}{2\pi E_{yy}}\right)^{1/2} \frac{K^{\infty}}{dE'}\sqrt{\xi} + \left(\frac{2G}{\pi E_{yy}}\right)^{1/2} \frac{\ell}{d}\frac{G}{E'} \int_0^1 \frac{T(\xi')}{G} \ln \left| \frac{\sqrt{\xi} + \sqrt{\xi'}}{\sqrt{\xi} - \sqrt{\xi'}} \right| \mathrm{d}\xi', \tag{4.12}$$

where $\xi \equiv x/\ell$ and $\xi' \equiv x'/\ell$.

In order to solve (4.12) we express $K^{\infty}$ as a function of the cohesive zone length $\ell$ by substituting (4.3) and (4.4) into (4.9), leading to the following integral equation in $T(\xi)$:

$$f^{-1}\left(\frac{T(\xi)}{G}\right) = \frac{\ell G^{3/2}}{dE' E_{yy}^{1/2}} \int_0^1 \left( -\frac{4}{\pi}\frac{T(\xi')}{G}\sqrt{\frac{\xi}{\xi'}} + \sqrt{\frac{2}{\pi}}\frac{T(\xi')}{G} \ln\left|\frac{\sqrt{\xi}+\sqrt{\xi'}}{\sqrt{\xi}-\sqrt{\xi'}}\right| \right) \mathrm{d}\xi'. \tag{4.13}$$

This equation is solved by dividing the cohesive zone into $N$ elements of equal length (typically, $N = 100$). The traction distribution within the cohesive zone is taken to be piece-wise linear, with triangular distributions of crack face traction with peak value $T_i$ centred on the $i$th node. The integrals in equation (4.13) are calculated numerically at the node points $\xi_i$ for triangular distributions of traction of unit magnitude at the $N$ node points. Equation (4.13) is expressed as $N$ simultaneous equations, containing these influence coefficients. The set of nonlinear algebraic equations for $T_i$ is solved using a modified Powell hybrid method in the form of a NAG subroutine (NAG 1986). The solution gives us the length of the cohesive zone $\ell$ as a function of $K^{\infty}$, which may be written in the following non-dimensional form:

$$\frac{\ell G^{3/2}}{dE' E_{yy}^{1/2}} = g\left(\frac{K^{\infty}}{d^{1/2}E'^{1/2}E_{yy}^{1/4}G^{1/4}}, \gamma_y, n, \beta, \frac{E_{xx}}{G}\right). \tag{4.14}$$

### (*c*) *Comparison of results of bridging analysis with finite element predictions*

The $R$-curves predicted by the cohesive zone model are compared with the $R$-curves from the finite element computations in figure 10*a* for $n$ in the range of 3.5 to 100, and in figure 10*b* for $\gamma_y$ in the range $9.2 \times 10^{-4}$ to $9.2 \times 10^{-2}$. Results are given for the full bridging laws displayed in figure 9 and for a simplified Dugdale bridging law of a constant bridging stress $\sigma_{\mathrm{b}}$ and a finite crack tip toughness $G_{\mathrm{tip}}$. The value of $\sigma_{\mathrm{b}}$ is set by the asymptotic value of $\sigma^{\infty}$ for large $\Delta v/d$ (taken here as $2\Delta v/d = 40$). $G_{\mathrm{tip}}$ is the area under the $(\sigma^{\infty} - \sigma_{\mathrm{b}})$ versus $2\Delta v$ curve; it is the area under the crack bridging curve additional to the contribution from the uniform traction $\sigma_{\mathrm{b}}$.

Consider first the results shown in figure 10*a* for the strain hardening parameter $n$ varying between 3.5 and 100. For $n = 3.5$, predictions using the simplified Dugdale bridging law agree very well with the finite element calculations, while the full cohesive zone bridging law calculation under-predicts the applied load by between 20 and 50% for a given microbuckle length as compared with the finite element calculation. Quantitative agreement between the finite element results and the Dugdale bridging law is less good for $n = 15$ and 100, although the qualitative effect of changes in $n$ are reproduced well by the bridging models, at least for large $\ell$.

Figure 10*b* illustrates the change in the predicted $R$-curve as the yield strain $\gamma_y$ changes by two orders of magnitude. There is good qualitative agreement between the predictions of the cohesive zone models and the finite element calculation, although again there are quantitative differences.

Figure 11 compares the stresses ahead of the crack tip found from the finite element calculations, from the simplified Dugdale model and from the full cohesive zone bridging model. Also shown is the elastic stress field. Results are at a load corresponding to state C of figures 3 and 4 with $n = 3.5$ and $\gamma_y = 9.2 \times 10^{-3}$. The bridging models both show a peak in stress at the tip of the microbuckle. This is a consequence of the high strength corresponding to the small fibre rotations at the

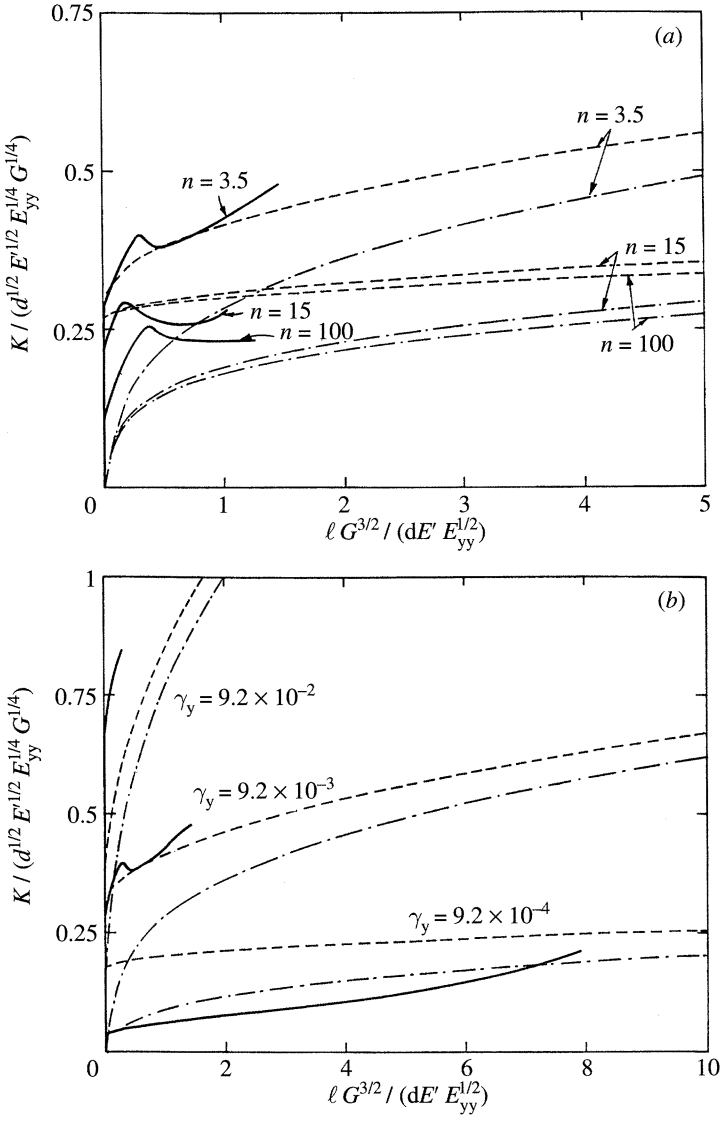


Figure 10. Comparison of $R$-curves calculated from cohesive zone and finite element calculations. ($a$) Effect of magnitude of strain hardening exponent $n$, for $\gamma_y = 9.2 \times 10^{-3}$; ($b$) effect of magnitude of yield strain $\gamma_y$, for $n = 3.5$. ——, finite element results; - - - -, simplified Dugdale model; — · — ·, full bridging law.

tip of the cohesive zone. In contrast the finite element calculation does not have a pronounced peak in stress. The stress distribution at the crack tip ($x = 0$) associated with microbuckling blends smoothly into the crack-tip field ahead of the microbuckle. At the crack tip the normalized microbuckle stress $\sigma/G$ is 0.15 while the predicted stress using the infinite band bridging law is approximately half this value. The detailed differences between the solutions shown in figure 11 explain the quantitative differences observed between the $R$-curves calculated from the cohesive zone models and the finite-element analysis.

The cohesive zone model assumes elastic behaviour outside the cohesive zone.

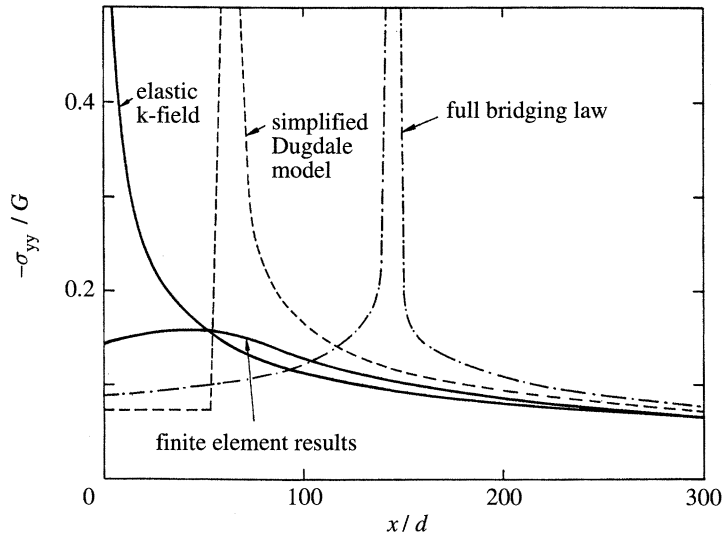


Figure 11. Comparison of the composite mean axial stress ahead of the crack tip calculated from the finite element and cohesive zone models. Mode-I loading with $\gamma_y = 9.2 \times 10^{-3}$ , $n = 3.5$ and $K_I/G\sqrt{d} = 2.8$, corresponding to state C of figure 3.

Examination of the stress state found in the finite element analysis reveals that the microbuckle is surrounded by a domain of plastic shear, mainly along the fibre direction. The above cohesive zone model suffers from the following deficiencies.

(i) The assumed bridging law considers only normal tractions with no influence of shear tractions on the bridging response. In fact the finite element results of figure 8*a* for mixed mode loading show that the effect of shear tractions is not straightforward and would not be well modelled by simple modification of the bridging response.

(ii) The cohesive zone model assumes elastic behaviour outside the cohesive zone. A more accurate model could be developed whereby the field beyond the cohesive zone is deforming plastically. Such an approach has been developed by Tvergaard & Hutchinson (1994) recently, but relies upon a finite element procedure for its implementation.

## 5. Conclusions

Finite element calculations have been used to predict initiation and the early stages of growth of a microbuckle from a crack. The microbuckle length has been estimated by finding where the stress ahead of the crack falls significantly below the stress for an elastic homogeneous material. *R*-curves (showing the dependence of the applied stress intensity factor on the microbuckle length) have been derived. In some cases this curve displays a local maximum: snap-back buckling occurs. The influence of matrix shear yield strain on the *R*-curve response is significant; the effect of strain-hardening exponent is relatively minor. The predicted microbuckle initiation load is found to be in good agreement with experimental data for a carbon fibre epoxy composite.

Waviness has only a slight influence on the details of the *R*-curve, rather than the dominant role found in the infinite-band collapse response. A small effect of waviness on the *R*-curve is consistent with the notion that the initial notch acts as a large imperfection in the structure, and induces waviness ahead of its tip. The finite

element calculations show that a mode-II component on the crack tip does not knock down the failure load significantly. This is in contrast to the infinite-band response, where shear knocks down the collapse load considerably.

A comparison has been made between the finite element calculations and bridging calculations wherein the infinite band collapse response is used to infer the $R$-curve. The bridging calculations adequately predict the effects of strain hardening and matrix yield strain on the $R$-curve, although the details of the stresses ahead of the crack tip are not accurately modelled.

The authors are grateful for helpful discussions with Dr P. T. Curtis at DRA Farnbourough and for financial support from the Procurement Executive of the Ministry of Defence, contract 2029/267, from the U.S. Office of Naval Research grant 0014-91-J-1916, and from the Nuffield Foundation.

## References

ABAQUS manual 1994 Version 5.3. Providence, RI: Hibbitt, Karlsson & Sorensen, Inc.

Argon, A. S. 1972 Fracture of composite. *Treatise of materials science and technology*, vol. 1. New York: Academic.

Awerbuch, J. & Madhukar, M. S. 1985 Notched strength in composite laminates: predictions and experiments—a review. *J. Reinforced Plastic Composites* **4**, 3–12.

Budiansky, B. 1983 Micromechanics. *Comput. Struct.* **16**, 3–12.

Budiansky, B. & Fleck, N. A. 1993 Compressive failure of fiber composites. *J Mech. Phys. Solids* **41**, 183–211.

Cox, B. N. & Marshall, D. B. 1991 *Acta Metall.* **39**, 579–589.

Fleck, N. A. & Budiansky, B. 1991 Compressive failure of fibre composites due to microbuckling. In *Inelastic deformation of composite materials* (ed. G. J. Dvorak), pp. 235–274. Berlin: Springer.

Fleck, N. A. Deng, L. & Budiansky, B. 1993 Prediction of kink widths in fiber composites. *J. Appl. Mech.* **62**, 329–337.

Fleck, N. A. & Shu, J.Y. 1995 Microbuckle initiation in fibre composites: a finite element study. *J. Mech. Phys. Solids* **43**, 1887–1918.

Jelf, P. M. & Fleck, N. A. 1994 The failure of composite tubes due to combined compression and torsion. *J. Mater. Science* **29**, 3080–3086.

Moran, P. M. Liu, X. H. & Shih, C. F. 1995 Kink band formation and band broadening in unidirectional fiber composites under compression loading. *Acta Metall.* **43**, 2943–2958.

NAG Fortran library manual—mark II. 1986 Oxford: Numerical Algorithms Group.

Nuismer, R. J. & Labor, J. D. 1979 Application of the average stress failure criterion. Part II. *Compression. J. Comp. Mater.* **13**, 49–69.

Paris, P. C. & Sih, G. C. 1969 Stress analysis of cracks. In *Fracture toughness applications*, ASTM STP 381, pp. 30–83.

Paris, P. C. McMeeking, R. M. & Tada, H. 1976 In *Cracks and fracture*, ASTM STP 601, pp. 471-489.

Peterson, R. E. 1974 *Stress concentration factors.* New York: Wiley.

Rhodes, M. D. Mikulas, M. M. & McGowan, P. E. 1984 Effects of orthotropy and width on the compression strength of graphite/epoxy panels with holes. *AIAA Jl* **22**, 1283–1292.

Shu, J. Y. & Fleck, N. A. 1996 Microbuckle initiation under multi-axial loading. *Proc. R. Soc. Lond.* A (Submitted.)

Sih, G. C. Paris, P. C. & Irwin, G. R. 1965 *Int. J. Fracture Mech.* **1**, 189–203.

Slaughter, W. S. Fleck, N. A. & Budiansky, B. 1993 Compressive failure of fiber composites; the roles of multi-axial loading and creep. *J. Engng Mater. Tech.* **115**, 308–313.

Soutis, C. & Fleck, N. A. 1990 Static compression failure of carbon fibre T800/924C composite plate with single hole. *J. Comp. Mater.* **24**, 536–558.

Soutis, C. Fleck, N. A. & Smith, P. A. 1991 Failure prediction technique for compression loaded carbon fibre-epoxy laminate with an open hole. *J. Comp. Mater.* **25**, 1476–1498.

Soutis, C. Curtis, P. T. & Fleck, N. A. 1993 Compressive failure of notched carbon fibre composites. *Proc. R. Soc. Lond.* A **440**, 241–256.

Sutcliffe, M. P. F. & Fleck, N. A. 1993 Effect of geometry on compressive failure of notched composites. *Int. J. Fract.* **59**, 115–132.

Sutcliffe, M. P. F. & Fleck, N. A. 1994 Microbuckle propagation in carbon fibre-epoxy composites. *Acta Metall.* **42**, 2219–2231.

Tada, H. Paris, P. C. & Irwin, G. R. 1985 *The stress analysis of cracks handbook*, 2nd edn. Paris Productions Inc.

Tvergaard, V. & Hutchinson, J. W. 1992 The relation between crack growth resistance and fracture process parameters in elastic-plastic solids. *J. Mech. Phys. Solids* **40**, 1377–1397.

Whitney, J. M. & Nuismer, R. J. 1974 Stress fracture criteria for laminated composites containing stress concentrations. *J. Comp. Mater.* **8**, 253–265.

Yurgatis, S. W. 1987 Measurement of small angle misalignments in continuous fibre composites. *Composites Sci. Technol.* **30**, 279–293.

*Received 29 June 1995; accepted 19 December 1995*